THE JOURNAL OF PHYSICAL CHEMISTRY C

pubs.acs.org/JPCC Article

Unit-Cell-Thick Oxide Synthesis by Film-Based Scavenging

Saloni Pendse, Jie Jiang, Yuwei Guo, Lifu Zhang, Zhizhong Chen, Zonghuan Lu, Yuandong Wang, Yang Hu, Songman Li, Jing Feng, Toh-Ming Lu, Yi-Yang Sun,* and Jian Shi*

Cite This: https://dx.doi.org/10.1021/acs.jpcc.0c00578 Read Online

ACCESS | Metrics & More | Article Recommendations | Supporting Information

ABSTRACT: With the influx of flexible electronics as well as the emergence or prediction of unique phenomena in two-dimensional forms of materials, epitaxy at weakly coupled interfaces is gaining momentum as a feasible technique to develop nanostructured and two-dimensional materials. The weak substrate−film chemical interaction expected in this method of epitaxy has been believed to be crucial in enabling not only the formation of sharp heterostructures but also the mechanical exfoliation of the epilayer. In this report, we unravel an unconventional understanding of epitaxy at weakly coupled interfaces, entailing ions of the van der Waals substrate being scavenged by the growing film, resulting in the formation of a distinct and uniform unit-cell-thick interfacial layer. Using a layered Dion−Jacobson perovskite as the substrate and VO_2 as the growing epilayer, we show that VO_2 scavenges ions from the substrate and forms an epitaxial vanadate compound. Additionally, the crystal anisotropy of the substrate significantly modifies the energy landscape for diffusion of ions and leads to the creation of a unit-cell-thick epitaxial Aurivillius phase at the interface, predicted to exhibit the ferroelectric Rashba−Dresselhaus effect. The scavenging effect, interfaced with an anisotropic low-dimensional substrate, opens a new window to develop two-dimensional flexible components for future electronics.

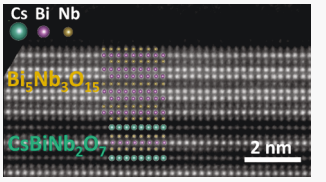

1. INTRODUCTION

Over the past several decades, oxide materials have been of significant research interest, especially for use in the field of electronics, owing to their extraordinary properties including multiferroicity, superconductivity, and magnetoresistance.[1] With the rapid miniaturization of electronics and the observation or prediction of unique scientific phenomena in nanoscale and atomic scale materials, there is also a drive to develop nanostructures or two-dimensional forms of oxides.[2−9] Additionally, with the advent of flexible electronics, further expansion of the scope of low-dimensional oxides lies in their growth on flexible, transferrable substrates making it easier for them to be integrated into devices.[9] Van der Waals (vdW) epitaxy, which facilitates growth of single-crystalline films on 2D-layered substrates without stringent lattice matching requirements is one technique being rigorously explored for such purposes.[10,11]

Recently, vdW epitaxy of oxide thin films via pulsed-laser deposition on flexible mica substrates has been reported. Transparent films of VO_2 exhibiting a metal−insulator transition,[12] films of Fe_3O_4 for flexible spintronics,[13] $CoFe_2O_4$ films for magnetostriction,[14,15] and flexible ferroelectric $PbZr_{0.2}Ti_{0.8}O_3$ films[16] on mica have all been successfully demonstrated. However, the obtained films are generally much thicker than 2D materials, limiting their applicability in exploring new physics and emerging applications. Growing ultrathin or 2D single-crystalline oxide films on vdW or the so-called quasi-vdW substrates (which form interfaces having ionic as well as a significant vdW character[17]) has been a challenge. This is in part because the weak film-substrate interaction in vdW epitaxy systems favors formation of islands and their subsequent coalescence as the dominant growth mechanism.[18] The other hurdle is from the common symmetry mismatch between hexagonal vdW substrates and cubic or pseudo cubic films. For example, it can be seen that mica, with its pseudo hexagonal atomic structure,[19] is lattice mismatched with respect to most complex oxides, including perovskites of tetragonal or orthorhombic symmetry. Therefore, it is necessary to scout out vdW materials with a cubic symmetry that can serve as appropriate substrates for epitaxy of single-crystalline oxide nanostructures. This served as the initial motivation behind our aim and is illustrated in Figure 1a−d. Symmetry-matching conditions in a hexagonal substrate-cubic film system are contrasted with those in a cubic substrate-cubic film system in Figure 1a,c, respectively. In this work, we use $CsBiNb_2O_7$ (CBNO), a Dion−Jacobson layered perovskite with orthorhombic symmetry (in-plane lattice constants a = 5.49 Å and b = 5.42 Å) as the quasi-vdW substrate[20] and VO_2, a strongly correlated oxide well-known for its near-room-temperature metal−insulator transition and having a tetragonal symmetry at growth temperatures[21,22] as a model oxide to grow ultrathin or 2D films. Figure 1b,d highlights the pseudo-hexagonal symmetry of mica,[19] a commonly used vdW substrate and the orthorhombic symmetry of CBNO, respectively. In keeping with the

Received: January 21, 2020
Revised: March 23, 2020
Published: March 26, 2020

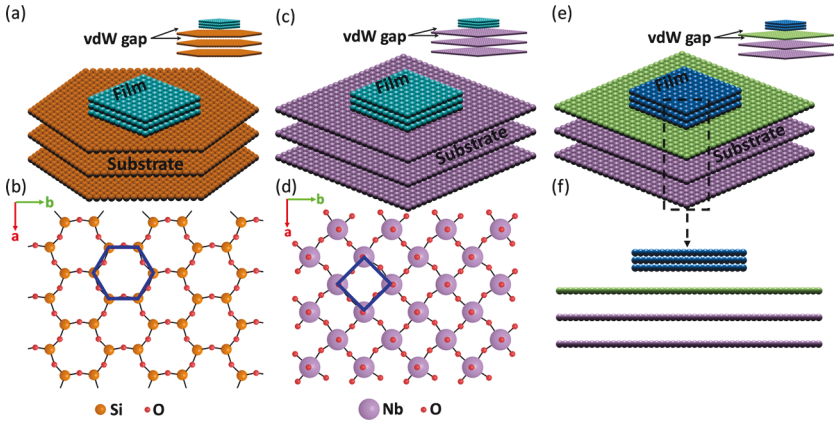

Figure 1. Van der Waals epitaxy in 3D/2D interface. (a) Schematic illustration of vdW epitaxy of a cubic film on a substrate with hexagonal atomic structure. (b) Atomic structure of cleaved surface of mica; a partial set of atoms has been represented for simplicity. (c) Schematic illustration of vdW epitaxy of a cubic film on a substrate with cubic atomic structure. (d) Top layer of $CsBiNb_2O_7$ (CBNO) (Projection onto *c*-axis), a partial set of atoms has been represented for simplicity. (e) Schematic illustration of possible film-substrate interaction in a vdW epitaxy system. (f) Side-view of (e) showing impact of film-substrate interaction on the growing film as well as the top layer of the vdW substrate. Insets show oblique views to highlight the vdW gap between substrate interlayers and across the film−substrate interface.

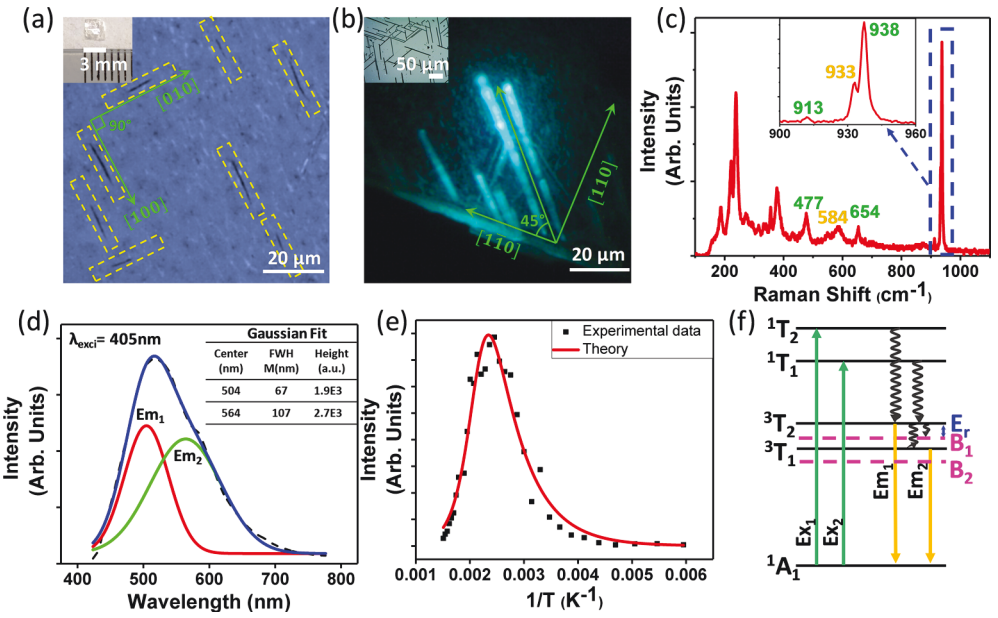

Figure 2. Photoluminescence in epitaxial $CsVO_3$ nanowires. (a) Optical image of epitaxial $CsVO_3$ nanowires. Inset shows a 3 mm×3 mm CBNO substrate. (b) Photoluminescence (PL) exhibited by the $CsVO_3$ nanowires. Inset shows epitaxial VO_2 nanowires on *c*-plane sapphire grown by the same recipe. (c) Raman analysis of the grown nanowires showing clear $CsVO_3$ peaks (highlighted in green) in addition to CBNO peaks (yellow). (d) Typical overall PL spectrum from the $CsVO_3$ nanowires and Gaussian fitting to resolve individual emissions. (e) Temperature-dependent study of intensity of Em_1 from 168 to 678 K. (f) Proposed electronic structure of the $CsVO_3$ nanowires where B_1 and B_2 are a defect related trap states.

assumption hitherto, that (i) interfaces in vdW or quasi-vdW epitaxy, unlike those in conventional epitaxy, are chemically sharp without any intermixing of elements, and (ii) based on the chemical and structural similarity between muscovite mica and CBNO, the film-substrate interface was initially expected to remain unaltered and abrupt.[9] Interestingly, however, growth results indicated otherwise. An attempt to grow VO_2 on CBNO resulted in the growth of $CsVO_3$ nanowires instead. After confirming the composition of the wires and studying their photoluminescence properties, structural analysis of the wire−substrate assembly revealed the presence of a distinct, uniform, and layered interface. This pointed to the presence of the film−substrate interaction in our quasi-vdW epitaxy system as illustrated in Figure 1e,f, which shows both the growing film and top layers of the substrate being impacted due to the film−substrate interaction. Here, we report our experimental observations of this phenomenon and their analysis by first-principles methods to determine the possible mechanism.

2. METHODS

2.1. Materials. Cesium carbonate powder (Cs_2CO_3, >99%), cesium chloride powder (CsCl, >99%), bismuth (III) oxide powder (Bi_2O_3, >99%), niobium (V) oxide powder (Nb_2O_5, >99%), and vanadium (IV) oxide powder (VO_2, >99%) were purchased from Sigma-Aldrich.

2.2. Molten Salt-Assisted Growth of CBNO. CBNO flakes, as shown in the inset of Figure 2a, were first synthesized by molten salt-assisted synthesis at 1173 K. Cs_2CO_3, Bi_2O_3,

https://dx.doi.org/10.1021/acs.jpcc.0c00578
J. Phys. Chem. C XXXX, XXX, XXX−XXX

and Nb_2O_5 precursor powders in a molar ratio of 3:2:4 were finely ground along with CsCl salt and packed in an alumina crucible. The weight ratio of CsCl solvent to all the precursors was 10:1. The crucible was placed in a horizontal furnace in open air, and the temperature was ramped in steps to 1173 K within 4 h, held for 4 h, and cooled slowly at a rate of 2 K/min. $CsBiNb_2O_7$ square crystals with a typical lateral size of ∼2 mm and a thickness of ∼0.2 mm were formed in the crucible and were thoroughly cleaned. Then, single crystals were exfoliated with scotch tape and transferred onto c-plane sapphire.

2.3. Chemical Vapor Deposition Using VO_2 Precursor. Chemical vapor deposition (CVD) was done in a tube furnace at 873 K using VO_2 as a precursor and CBNO flakes or c-plane sapphire as the substrate. The precursor and substrate were placed in a quartz tube with an outer diameter of 1 in. and loaded into a single-zone horizontal tube furnace. Typically, the precursor and substrate were placed in close proximity to one another and about 10 cm upstream of the zone center. The furnace was pumped to a base pressure of ∼1 Torr after which 30 sccm Ar was flowed in to establish a pressure of 5 Torr. The zone center was then ramped to 873 K within 20 min and dwelled at 873 K for 3−4 h. After the end of the heating cycle, Ar flow was maintained while the furnace naturally cooled to room temperature.

2.4. Characterization. *2.4.1. Imaging.* The resulting wires were studied using optical microscopy (Ti-S Nikon inverted microscope) and scanning electron microscopy (SEM) (Zeiss Supra 55 system).

2.4.2. Composition. Raman spectroscopy (Renishaw 2000 Raman spectrometer under a 540 nm laser), Raman mapping (Witec Alpha 300R confocal Raman imaging system), and energy-dispersive spectra (EDS) of the wires (Zeiss Supra 55 system) revealed the composition of the wires to be $CsVO_3$.

2.4.3. Photoluminescence. Photoluminescence (PL) properties of the $CsVO_3$ wires were studied using a customized system consisting of a Picoquant 405 nm pulsed diode laser, a Nikon Eclipse Ti-S inverted optical microscope, a Thorlabs 4 megapixel monochrome scientific CCD camera, and a Princeton Instruments SP-2358 spectrograph. The laser was focused onto a point on a nanowire, and signal was collected immediately. To collect temperature-dependent PL spectra, an INSTEC HCS302 temperature stage was used. Samples were glued to the stage with silver paste, and PL spectra were collected by loading the stage onto the optical microscope. A temperature range of 168−678 K was scanned in intervals of 15 K. Laser intensity was ∼2 mW. The obtained PL spectra were fitted with two Gaussian peaks corresponding to Em_1 and Em_2.

2.4.4. Structure. Structural analysis of the $CsVO_3$ wires was carried out using cross-sectional high-resolution transmission electron microscopy (HR-TEM) and selected-area electron diffraction (SAED) on a FEI F20 TEM operated at 200 kV. A Helios G4 UX focused ion beam (FIB) system was used to cut a lengthwise cross-section of the nanowire. The interface observed between the wire and substrate in TEM micrographs was further analyzed by collecting high-angle annular dark-field aberration-corrected scanning transmission electron microscopy (HAADF-STEM) images using a 300 kV FEI Titan Themis system.

2.4.5. First-Principles Calculations. The mechanism for the formation of this $Bi_5Nb_3O_{15}$ interfacial layer was probed by first-principles calculations to determine the diffusion barrier of Cs in CBNO along different directions. The calculations were based on density functional theory with a PBEsol functional[23] using the VASP package.[24] The optimized lattice constants of CBNO were a = 5.468 Å, b = 5.393 Å, and c = 11.424 Å. To obtain the barriers, the nudged elastic band (NEB) method[25] was used with three intermediate images.

3. RESULTS AND DISCUSSION

CVD using VO_2 as a precursor and CBNO as a substrate resulted in the growth of in-plane epitaxial nanowires along two perpendicular directions, i.e., either the a or b axis of CBNO, easily determined by a comparison with the edges of the CBNO substrate (Figure 2a,b). The temperature for CVD, i.e., 873 K, was determined keeping in mind the thermal stability of CBNO substrates and the VO_2 precursor. It was observed that CBNO substrates were not stable at growth temperatures in excess of ∼923 K. On the other hand, high thermal stability of VO_2 (mp: 1815 K)[26,27] necessitated a temperature of ∼873 K or more for growth. The pressure in the tube furnace was maintained at the lowest value (1 Torr) achievable in our set up to ensure uniformity of growth. The same recipe was followed to grow VO_2 on c-plane sapphire that resulted in the growth of epitaxial nanowires along three equivalent directions[28] as shown in the inset of Figure 2b. However, nanowires on the two different substrates differed in the sense that those on CBNO exhibited a broad PL peak as shown in Figure 2b. Further, analysis of the nanowires on CBNO by Raman spectroscopy indicated the absence of clear VO_2 peaks and instead revealed several $CsVO_3$ peaks in addition to CBNO peaks as highlighted in green and yellow in Figure 2c.[29,30] On the other hand, nanowires grown on c-plane sapphire exhibited strong VO_2 peaks (shown in the Supporting Information, Figure S1d). $CsVO_3$ is a well-known rare-earth-free luminescent material being explored for use in white-light LEDs and exhibits broad-band luminescence similar to our observation presented in Figure 2d.[31] The broad PL peak can be separated into two Gaussian peaks, with central wavelengths at 504 and 564 nm and hereafter referred to as Em_1 and Em_2, respectively (see the Supporting Information Note 1 for further details about the electronic structure and luminescence in $CsVO_3$). To further understand the origin of luminescence, PL of the $CsVO_3$ nanowires was probed by a temperature-dependent study of PL intensity. The CBNO−$CsVO_3$ assembly was subjected to temperatures ranging from 168 to 678 K, and PL spectra were collected at intervals of 15 K. The integrated PL intensities of Em_1 and Em_2 were then calculated and plotted against temperature. Results for Em_1 are as shown in Figure 2e, and those for Em_2 are shown in the Supporting Information, Figure S1f. The electronic structure of the grown $CsVO_3$ nanowires was modelled to fit the results obtained.

It can be seen that at high temperatures, the PL intensity decreased with increasing temperature, a phenomenon termed as "thermal quenching" of PL and commonly displayed by luminescent semiconducting or ionic materials due to increase in the probability of nonradiative thermal recombination with increasing thermal fluctuations. However, at low temperatures the PL intensity increased with increasing temperature. This is termed as "negative thermal quenching" of PL and is indicative of the presence of trap states within the band gap from which electrons can be thermally excited to a high-energy state before recombining and resulting in PL. Assuming there is one channel of nonradiative recombination with an energy barrier E_{nr} and one mid-gap state at an energy E_r below the excited

https://dx.doi.org/10.1021/acs.jpcc.0c00578
J. Phys. Chem. C XXXX, XXX, XXX−XXX

energy state of electrons, the intensity of PL as a function of temperature can be expressed as[32]

$$I(T) = \frac{I(0)\left[1 + C\exp\left(-\frac{E_r}{k_B T}\right)\right]}{\left[1 + D\exp\left(-\frac{E_{nr}}{k_B T}\right)\right]} \quad (1)$$

Here, $I(0)$ is the PL intensity at 0 K, k_B is the Boltzmann constant and, C and D are the relative contributions from the negative and positive thermal quenching effects, respectively. Experimental data was fit based on eq 1 as shown in Figure 2e, and the following parameters were obtained for peak Em_1: $I(0)$ = 100 arbitrary units (a.u.), C = 115621, E_r = 145 meV, D = 661456, and E_{nr} = 527 meV. Based on the above analysis of peaks Em_1 and Em_2 and the theoretical electronic structure of AVO_3 (A = Cs, Rb, K) compounds,[33] the electronic structure of the grown $CsVO_3$ nanowires can be represented as shown in Figure 2f. The mid-gap defect states B_1 and B_2 trap electrons, which can be excited to $^3T_2$ level and result in increased PL intensity as the temperature increases. Once the temperature is large enough to overcome the energy barrier for nonradiative recombination, E_{nr}, PL intensity drops with further increase in temperature.

Results of structural analysis of the nanowires carried out via lengthwise cross-sectional HR-TEM are presented in Figure 3. It can be seen from Figure 3a that the cross-section consisted of three distinct regions - (001) planes of the layered CBNO substrate, a uniform-layered interface, and crystalline $CsVO_3$. The interface was determined to be ∼1 unit-cell-thick $Bi_5Nb_3O_{15}$ (BNO) (further described in the following discussion). The top left and bottom right insets show SAED patterns collected from $CsVO_3$ and CBNO, respectively. Figure 3b shows a schematic drawing of the three distinct regions in Figure 3a and highlights the observed planes. Further analysis of $CsVO_3$ revealed the presence of regions with different but inter-related orientations. Two typical cases are presented here (see Figures S3 and S4 in the Supporting Information for additional images and analysis). Figure 3c and its right inset show the interface between two regions with different orientations viewed at high and low magnification, respectively. The orientation and epitaxial relations of both the regions were determined by fast Fourier transform (FFT) (see the Supporting Information, Figure S2) as $[\bar{1}01]$ $CsVO_3$ ∥ [001] BNO and (020) $CsVO_3$ ∥ (100) BNO (left) and $[\bar{3}11]$ $CsVO_3$ ∥ [001] BNO and $(\bar{1}30)$ $CsVO_3$ ∥ (100) BNO (right). Inverse FFT (left inset) revealed the presence of dislocations at the interface. A spacing of ∼22 atomic planes between successive dislocations corresponded well with the expected lattice mismatch of ∼6% between (040) and $(\bar{1}30)$ $CsVO_3$ planes (d_{040} = 3.05 Å and $d\bar{1}30$=3.24 Å). Figure 3d shows the corresponding $CsVO_3$ unit cells in their expected orientation and highlights the planes (040) and $(\bar{1}30)$ matching across the interface. The other typically seen relation between regions of different orientation was that of twinning, as shown in Figure 3e at high magnification and in its right inset at a lower magnification while the left inset shows an inverse FFT around the interface. Epitaxial relations of the two regions with respect to BNO were determined as $[\bar{1}01]$ $CsVO_3$ ∥ [001] BNO and (111) $CsVO_3$ ∥ (100) BNO for the left region and $[\bar{1}01]$ $CsVO_3$ ∥ [001] BNO and $(1\bar{1}1)$ $CsVO_3$ ∥ (001) BNO for the right region. Figure 3f shows the corresponding unit cells and

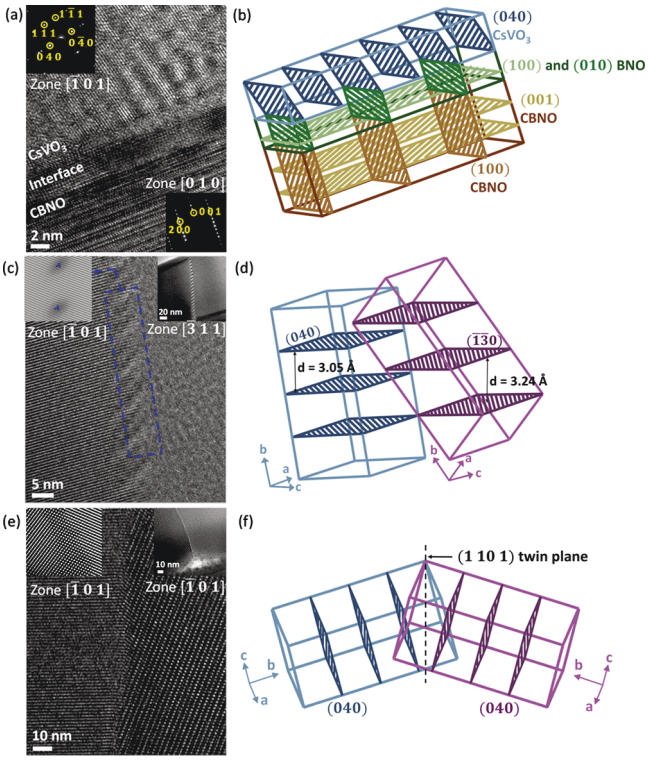

Figure 3. Structural analysis of epitaxial $CsVO_3$ nanowires. (a) Typical HR-TEM cross-section of $CsVO_3$ nanowire−CBNO substrate assembly revealing a distinct interface. Insets show SAED patterns of $CsVO_3$ (top left) and CBNO (bottom right). (b) Schematic representation of unit cell orientation of $CsVO_3$ as seen in (a). (c) Interdomain interface in $CsVO_3$ characterized by dislocations and analyzed by inverse fast Fourier transform (left inset). Right inset shows a low-magnification image of the interface. (d) $CsVO_3$ unit cells corresponding to regions in (c) and their planes matching across the interface. (e) Interdomain interface characterized by twinning. Insets show twinned lattice planes across the interface constructed by inverse fast Fourier transform (left) and a low-magnification image of the interface (right). (f) Schematic representation of twinned $CsVO_3$ unit cells corresponding to (e).

highlights their mirror symmetry across the (1 10 1) twinning plane.

As seen from HR-TEM, the $CsVO_3$ nanowires exhibit regions with different orientations and are not single crystalline in nature. This can be a result of island-type growth typically seen in vdW epitaxy[18] followed by oriented attachment of the islands or nanocrystals to form nanowires often seen in solution growth of nanostructures.[34] Individual islands or clusters can form in initial stages of growth due to weak interlayer bonding in vdW substrates. Similar to grains observed in graphene grown from SiC, the orientation of such individual nanocrystals can vary due to lattice matching considerations and simultaneous reconstruction of the substrate surface as a result of the scavenging effect of VO_2[35] (more details are discussed later). Further, aggregation of the independent, nearby nanocrystals is favored for minimization of surface energy and a drive to eliminate high-energy facets can lead to oriented aggregation into unique morphologies such as rods and wires as opposed to random aggregation.[34] Such oriented attachment is characterized by defects such as dislocations, stacking faults, and twins, which were observed in the $CsVO_3$ nanowires via HR-TEM. The interface seen in Figure 3a was further analyzed by HAADF-STEM and a

https://dx.doi.org/10.1021/acs.jpcc.0c00578
J. Phys. Chem. C XXXX, XXX, XXX−XXX

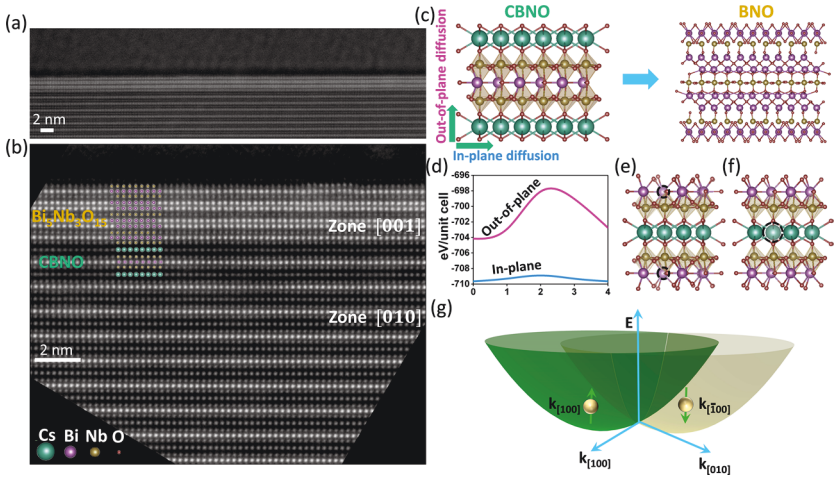

Figure 4. Unit-cell-thick $Bi_5Nb_3O_{15}$. (a) Wide-area STEM cross-section of $CsVO_3$ nanowire-CBNO substrate interface revealing a sharp, uniform, and layered interface. (b) Higher magnification view of the interface along with overlaid atomic structures of CBNO and $Bi_5Nb_3O_{15}$ (BNO). (c) Atomic structure of CBNO transforming into BNO via loss of Cs ions. (d) Out-of-plane and in-plane diffusion barrier for Cs ions. (e) Bi vacancy supercell for out-of-plane Cs diffusion. (f) Cs vacancy supercell for in-plane Cs diffusion and (g) Potential E-k dispersion with spin texture induced by the Rashba-Dresselhaus effect in $Bi_5Nb_3O_{15}$. The energy degeneracy of electrons with spin along [001] and [010] was lifted by the spin orbit field. See main text for more details.

uniform, layered interface was observed as shown in Figure 4a. The structure of CBNO substrate consists of Bi atoms (brightest) bounded by Nb atoms on either side. The Nb-Bi-Nb planes are interconnected by Cs ions, forming the layered structure of CBNO as shown in Figure 4a and highlighted in Figure 4b. The interface on the other hand shows a distinctly different structure consisting of alternating $(Bi_2O_2)^{2+}$ layers and NbO_6 octahedra stacks, both structural elements characteristic of Aurivillius perovskite phases $Bi_2A_{m-1}B_mO_{3m+1}$. The exact structure of the interface can be matched to ~1 unit-cell-thick $Bi_5Nb_3O_{15}$ [a = 21.01 Å, b = 5.47 Å, c = 5.46 Å], a mixed layer Aurivillius phase comprising Bi_2NbO_6 and $Bi_3Nb_2O_9$ layers stacked alternately, and studied for its ferroelectric, photocatalytic, and optoelectronic properties.[36−38] The growth of epitaxial $CsVO_3$ and formation of a unit-cell-thick $Bi_5Nb_3O_{15}$ interface may be understood by looking at the growth of epitaxial graphene by thermal decomposition of a bulk SiC substrate. Subjecting SiC crystals to temperatures in excess of 2453 K in an UHV environment or 1923 K in an Ar environment leads to evaporation of Si, leaving behind a complex C-rich interfacial layer, which then acts as a buffer or template layer for the growth of layers of graphene in the form of grains or domains.[35,39−41]

Similarly, for the vdW material CBNO, temperatures around 873 K and the scavenging effect of VO_2 during chemical vapor deposition can lead to the loss of the loosely bound Cs ions and result in the formation of a Bi and Nb rich buffer or interface layer (BNO). As this process requires that Cs atoms diffuse out of CBNO, we calculated the diffusion barriers for Cs in CBNO by first principles methods along two possible paths, one path being vertical or out-of-plane diffusion across two Nb−O perovskite layers mediated by a Bi vacancy in the Bi layer and the other being lateral or in-plane diffusion mediated by a Cs vacancy. The results are presented in Figure 4d−f, and it can be seen that the out-of-plane diffusion barrier (~6.4 eV/unit cell) is significantly larger than the in-plane diffusion barrier (~0.75 eV/unit cell). This energy barrier anisotropy may be the underlying reason for the formation of a uniform, unit-cell-thick $Bi_5Nb_3O_{15}$ interfacial layer: the large energy barrier along c-direction prevents the out-of-plane Cs loss and the long diffusion length along the in-plane direction also limits the Cs loss. As such, the scavenging effect of VO_2, i.e., the transformation of CBNO into BNO by Cs loss is curtailed and only a unit-cell-thick layer of interfacial BNO is formed. This is in contrast to graphene synthesis by Si loss from SiC where multilayer graphene or graphite formation is commonly observed and may be due to the isotropic structure of SiC.

The polar space group Pnc2 of $Bi_5Nb_3O_{15}$, together with the strong spin−orbit coupling effect introduced by heavy element Bi would lead to an interesting phenomenon, the Rashba−Dresselhaus effect. This effect has been traditionally explored in semiconducting materials lacking inversion symmetry (either intrinsically or introduced by geometrical modification).[42,43] Recently, to explore its application in spintronics, researchers have proposed the use of ferroelectricity to tune the spin polarization in a nonvolatile manner, opening a new window for low-power electronics, and computing.[44,45] Among all candidates, ferroelectric oxides with strong spin−orbit coupling have been theoretically formulated to be promising.[46] Our synthesized $Bi_5Nb_3O_{15}$ satisfies such requirements and its low-dimensional morphology may further reduce the electron−phonon coupling and in turn prolong the lifetime of spin polarization. Figure 4g shows the proposed spin-polarized band structure due to the relativistic electron effect in this Rashba−Dresselhaus system. The spin polarization is formulated by a [110]-Dresselhaus model.[47] Based on this model, the band dispersion will follow a formulation of $\hat{H} = \frac{\hbar^2}{2m^*}(k_z^2 + k_y^2) + \alpha_R k_y \sigma_x$ (σ_x: Pauli matrix). Efforts to experimentally realize the spin-polarized band structure via the circular photogalvanic effect (CPGE)[48] are currently underway.

4. CONCLUSIONS

In summary, we attempted vdW epitaxy of VO_2 on $CsBiNb_2O_7$ (CBNO), a Dion−Jacobson oxide perovskite, which in turn resulted in the growth of $CsVO_3$ nanowires and the development of a ~1 unit-cell-thick $Bi_5Nb_3O_{15}$ (BNO)

https://dx.doi.org/10.1021/acs.jpcc.0c00578
J. Phys. Chem. C XXXX, XXX, XXX−XXX

mixed-layer Aurivillius substrate−wire interface possibly due to the scavenging effect of VO_2 aided by the anisotropic structure of CBNO. Hence, it may be said that significant chemical film−substrate interaction is possible in vdW epitaxy systems. Weak interlayer bonding can make vdW substrates susceptible to scavenging of ions by precursor materials, which can impact not only the film-substrate interface but also the growing film itself. Additionally, weak vdW bonding at the film−substrate interface can enable growth by oriented attachment, a growth mechanism otherwise only common in solutions, and characterized by regions of different orientation exhibiting interfacial dislocations or twinning. A thorough understanding of the above-mentioned phenomena in vdW epitaxy systems is important not only from a scientific point of view but also for effectively using them as a means to develop low-dimensional materials, such as the unit-cell-thick $Bi_5Nb_3O_{15}$ formed in our system with a promising ferroelectric field-controlled Rashba-Dresselhaus effect for future spintronics.

■ ASSOCIATED CONTENT

Supporting Information

The Supporting Information is available free of charge at https://pubs.acs.org/doi/10.1021/acs.jpcc.0c00578.

Structure, spectroscopy, EDX and photoluminescence of epitaxial nanowires, and microscopy images and analyses (PDF)

■ AUTHOR INFORMATION

Corresponding Authors

Yi-Yang Sun − *State Key Laboratory of High Performance Ceramics and Superfine Microstructure, Shanghai Institute of Ceramics, Chinese Academy of Sciences, Shanghai 201899, China;* orcid.org/0000-0002-0356-2688; Email: yysun@mail.sic.ac.cn

Jian Shi − *Department of Materials Science and Engineering and Center for Materials, Devices and Integrated Systems, Rensselaer Polytechnic Institute, Troy, New York 12180, United States;* orcid.org/0000-0003-2115-2225; Email: shij4@rpi.edu

Authors

Saloni Pendse − *Department of Materials Science and Engineering, Rensselaer Polytechnic Institute, Troy, New York 12180, United States*

Jie Jiang − *Department of Materials Science and Engineering, Rensselaer Polytechnic Institute, Troy, New York 12180, United States; Faculty of Materials Science and Engineering, Kunming University of Science and Engineering, Kunming 650093, China*

Yuwei Guo − *Department of Materials Science and Engineering, Rensselaer Polytechnic Institute, Troy, New York 12180, United States*

Lifu Zhang − *Department of Materials Science and Engineering, Rensselaer Polytechnic Institute, Troy, New York 12180, United States*

Zhizhong Chen − *Department of Materials Science and Engineering, Rensselaer Polytechnic Institute, Troy, New York 12180, United States*

Zonghuan Lu − *Department of Physics, Applied Physics and Astronomy, Rensselaer Polytechnic Institute, Troy, New York 12180, United States;* orcid.org/0000-0003-2375-8247

Yuandong Wang − *State Key Laboratory of High Performance Ceramics and Superfine Microstructure, Shanghai Institute of Ceramics, Chinese Academy of Sciences, Shanghai 201899, China; University of Chinese Academy of Sciences, Beijing 100049, China*

Yang Hu − *Department of Materials Science and Engineering, Rensselaer Polytechnic Institute, Troy, New York 12180, United States*

Songman Li − *Emma Willard School, Troy, New York 12180, United States*

Jing Feng − *Faculty of Materials Science and Engineering, Kunming University of Science and Engineering, Kunming 650093, China*

Toh-Ming Lu − *Department of Physics, Applied Physics and Astronomy, Rensselaer Polytechnic Institute, Troy, New York 12180, United States*

Complete contact information is available at: https://pubs.acs.org/10.1021/acs.jpcc.0c00578

Notes

The authors declare no competing financial interest.

All data needed to evaluate the conclusions in the paper are presented in the paper and/or the Supporting Information. Additional data related to this paper may be requested from the authors.

■ ACKNOWLEDGMENTS

This material is based upon work supported by the Air Force Office of Scientific Research under award number FA9550-18-1-0116, National Science Foundation under award numbers 1706815 and 1916652, and the NYSTAR Focus Center under award number C150117. We also thank RPI Cleanroom and nanofabrication facility for device fabrication.

■ REFERENCES

(1) Mannhart, J.; Schlom, D. G. Oxide Interfaces — An Opportunity for Electronics. *Science* **2010**, *327*, 1607−1611.

(2) Yang, T.; Song, T. T.; Callsen, M.; Zhou, J.; Chai, J. W.; Feng, Y. P.; Wang, S. J.; Yang, M. Atomically Thin 2D Transition Metal Oxides: Structural Reconstruction, Interaction with Substrates, and Potential Applications. *Adv. Mater. Interfaces* **2019**, *6*, 1801160.

(3) Diao, F.; Wang, Y. Transition Metal Oxide Nanostructures: Premeditated Fabrication and Applications in Electronic and Photonic Devices. *J. Mater. Sci.* **2018**, *53*, 4334−4359.

(4) Chan, L. H.; Yuhara, J. Epitaxial Growth and Structure of Monolayer Cerium Oxide Films on Rh(111). *Surf. Sci.* **2017**, *661*, 69−76.

(5) Surnev, S.; Vitali, L.; Ramsey, M. G.; Netzer, F. P.; Kresse, G.; Hafner, J. Growth and Structure of Ultrathin Vanadium Oxide Layers on Pd(111). *Phys. Rev. B* **2000**, *61*, 13945−13954.

(6) Dai, Z. R.; Pan, Z. W.; Wang, Z. L. Novel Nanostructures of Functional Oxides Synthesized by Thermal Evaporation. *Adv. Funct. Mater.* **2003**, *13*, 9−24.

(7) Ji, D.; Cai, S.; Paudel, T. R.; Sun, H.; Zhang, C.; Han, L.; Wei, Y.; Zang, Y.; Gu, M.; Zhang, Y.; et al. Freestanding Crystalline Oxide Perovskites down to the Monolayer Limit. *Nature* **2019**, *570*, 87−90.

(8) Hong, S. S.; Yu, J. H.; Lu, D.; Marshall, A. F.; Hikita, Y.; Cui, Y.; Hwang, H. Y. Two-Dimensional Limit of Crystalline Order in Perovskite Membrane Films. *Sci. Adv.* **2017**, *3*, eaao5173.

(9) Chu, Y. H. Van Der Waals Oxide Heteroepitaxy. *npj Quantum Mater.* **2017**, *2*, 1−5.

(10) Kim, Y.; Cruz, S. S.; Lee, K.; Alawode, B. O.; Choi, C.; Song, Y.; Johnson, J. M.; Heidelberger, C.; Kong, W.; Choi, S.; et al. Remote Epitaxy through Graphene Enables Two-Dimensional Material-Based Layer Transfer. *Nature* **2017**, *544*, 340−343.

(11) Huang, J.; Wang, H.; Sun, X.; Zhang, X.; Wang, H. Multifunctional La0.67Sr0.33MnO3 (LSMO) Thin Films Integrated

on Mica Substrates toward Flexible Spintronics and Electronics. *ACS Appl. Mater. Interfaces* **2018**, *10*, 42698−42705.
(12) Li, C.-I.; Lin, J.-C.; Liu, H.-J.; Chu, M.-W.; Chen, H.-W.; Ma, C.-H.; Tsai, C.-Y.; Huang, H.-W.; Lin, H.-J.; Liu, H.-L.; et al. Van Der Waal Epitaxy of Flexible and Transparent VO2Film on Muscovite. *Chem. Mater.* **2016**, *28*, 3914−3919.
(13) Wu, P.-C.; Chen, P.-F.; Do, T. H.; Hsieh, Y.-H.; Ma, C.-H.; Ha, T. D.; Wu, K.-H.; Wang, Y.-J.; Li, H.-B.; Chen, Y.-C.; et al. Heteroepitaxy of Fe3O4/Muscovite: A New Perspective for Flexible Spintronics. *ACS Appl. Mater. Interfaces* **2016**, *8*, 33794−33801.
(14) Liu, H.-J.; Wang, C.-K.; Su, D.; Amrillah, T.; Hsieh, Y.-H.; Wu, K.-H.; Chen, Y.-C.; Juang, J.-Y.; Eng, L. M.; Jen, S.-U.; et al. Flexible Heteroepitaxy of CoFe2O4/Muscovite Bimorph with Large Magnetostriction. *ACS Appl. Mater. Interfaces* **2017**, *9*, 7297−7304.
(15) Amrillah, T.; Bitla, Y.; Shin, K.; Yang, T.; Hsieh, Y.-H.; Chiou, Y.-Y.; Liu, H.-J.; Do, T. H.; Su, D.; Chen, Y.-C.; et al. Flexible Multiferroic Bulk Heterojunction with Giant Magnetoelectric Coupling via van Der Waals Epitaxy. *ACS Nano* **2017**, *11*, 6122−6130.
(16) Jiang, J.; Bitla, Y.; Huang, C.-W.; Do, T. H.; Liu, H.-J.; Hsieh, Y.-H.; Ma, C.-H.; Jang, C.-Y.; Lai, Y.-H.; Chiu, P.-W.; et al. Flexible Ferroelectric Element Based on van Der Waals Heteroepitaxy. *Sci. Adv.* **2017**, *3*, e1700121.
(17) Wang, Y.; Gao, L.; Yang, Y.; Xiang, Y.; Chen, Z.; Dong, Y.; Zhou, H.; Cai, Z.; Wang, G.-C.; Shi, J. Nontrivial Strength of van Der Waals Epitaxial Interaction in Soft Perovskites. *Phys. Rev. Mater.* **2018**, *2*, 1−8.
(18) Geim, A. K.; Grigorieva, I. V. Van Der Waals Heterostructures. *Nature* **2013**, *499*, 419−425.
(19) Ostendorf, F.; Schmitz, C.; Hirth, S.; Kühnle, A.; Kolodziej, J. J.; Reichling, M. How Flat Is an Air-Cleaved Mica Surface? *Nanotechnology* **2008**, *19*, 305705.
(20) Chen, C.; Ning, H.; Lepadatu, S.; Cain, M.; Yan, H.; Reece, M. J. Ferroelectricity in Dion-Jacobson ABiNb2O7 (A = Rb, Cs) Compounds. *J. Mater. Chem. C* **2015**, *3*, 19−22.
(21) Ruzmetov, D.; Senanayake, S. D.; Narayanamurti, V.; Ramanathan, S. Correlation between Metal-Insulator Transition Characteristics and Electronic Structure Changes in Vanadium Oxide Thin Films. *Phys. Rev. B* **2008**, *77*, 195442.
(22) Whittaker, L.; Patridge, C. J.; Banerjee, S. Microscopic and Nanoscale Perspective of the Metal-Insulator Phase Transitions of VO2: Some New Twists to an Old Tale. *J. Phys. Chem. Lett.* **2011**, *2*, 745−758.
(23) Perdew, J. P.; Ruzsinszky, A.; Csonka, G. I.; Vydrov, O. A.; Scuseria, G. E.; Constantin, L. A.; Zhou, X.; Burke, K. Restoring the Density-Gradient Expansion for Exchange in Solids and Surfaces. *Phys. Rev. Lett.* **2008**, *100*, 136406.
(24) Kresse, G. Ab Initio Molecular Dynamics for Liquid Metals. *J. Non-Cryst. Solids* **1995**, *192-193*, 222−229.
(25) Henkelman, G.; Uberuaga, B. P.; Jónsson, H. A Climbing Image Nudged Elastic Band Method for Finding Saddle Points and Minimum Energy Paths. *J. Chem. Phys.* **2000**, *113*, 9901−9904.
(26) Yamaguchi, I.; Manabe, T.; Tsuchiya, T.; Nakajima, T.; Sohma, M.; Kumagai, T. Preparation and Characterization of Epitaxial VO2 Films on Sapphire Using Postepitaxial Topotaxy Route via Epitaxial V2O3 Films. *Jpn. J. Appl. Phys.* **2008**, *47*, 1022−1027.
(27) Ye, H.; Wang, H.; Cai, Q. Two-Dimensional VO2 Photonic Crystal Selective Emitter. *J. Quant. Spectrosc. Radiat. Transfer* **2015**, *158*, 119−126.
(28) Sohn, J. I.; Joo, H. J.; Porter, A. E.; Choi, C.-J.; Kim, K.; Kang, D. J.; Welland, M. E. Direct Observation of the Structural Component of the Metal-Insulator Phase Transition and Growth Habits of Epitaxially Grown VO2 Nanowires. *Nano Lett.* **2007**, *7*, 1570−1574.
(29) Kourouklis, G. A.; Jayaraman, A.; Espinosa, G. P.; Cooper, A. S. High-Pressure Raman Study of CsVO3 and Pressure-Induced Phase Transitions. *J. Raman Spectrosc.* **1991**, *22*, 57−60.
(30) Jehng, J. M.; Wachs, I. E. Structural Chemistry and Raman Spectra of Niobium Oxides. *Chem. Mater.* **1991**, *3*, 100−107.
(31) Pavitra, E.; Raju, G. S. R.; Bharat, L. K.; Park, J. Y.; Kwak, C. H.; Chung, J. W.; Han, Y.-K.; Huh, Y. S. Evolution of Highly Efficient Rare-Earth Free Cs(1-: X)RbxVO3 Phosphors as a Single Emitting Component for NUV-Based White LEDs. *J. Mater. Chem. C* **2018**, *6*, 12746−12757.
(32) Shibata, H. Negative Thermal Quenching Curves in Photoluminescence of Solids. *Jpn. J. Appl. Phys.* **1998**, *37*, 550−553.
(33) Nakajima, T.; Isobe, M.; Tsuchiya, T.; Ueda, Y.; Kumagai, T. Direct Fabrication of Metavanadate Phosphor Films on Organic Substrates for White-Light-Emitting Devices. *Nat. Mater.* **2008**, *7*, 735−740.
(34) Yong, K.-T.; Sahoo, Y.; Zeng, H.; Swihart, M. T.; Minter, J. R.; Prasad, P. N. Formation of ZnTe Nanowires by Oriented Attachment. *Chem. Mater.* **2007**, *19*, 4108−4110.
(35) Mishra, N.; Boeckl, J.; Motta, N.; Iacopi, F. Graphene Growth on Silicon Carbide: A Review. *Phys. Status Solidi* **2016**, *213*, 2277−2289.
(36) Tahara, S.; Shimada, A.; Kumada, N.; Sugahara, Y. Characterization of Bi5Nb3O15 by Refinement of Neutron Diffraction Pattern, Acid Treatment and Reaction of the Acid-Treated Product with n-Alkylamines. *J. Solid State Chem.* **2007**, *180*, 2517−2524.
(37) Boullay, P.; Palatinus, L.; Barrier, N. Precession Electron Diffraction Tomography for Solving Complex Modulated Structures: The Case of Bi5Nb3O15. *Inorg. Chem.* **2013**, *52*, 6127−6135.
(38) Gurunathan, K.; Maruthamuthu, P. Bi5Nb3O15 as a Photocatalyst: Photocatalytic and Photoelectrochemical Studies. *J. Solid State Electrochem.* **1998**, *2*, 176−180.
(39) Norimatsu, W.; Kusunoki, M. Growth of Graphene from SiC{0001} Surfaces and Its Mechanisms. *Semicond. Sci. Technol.* **2014**, *29*, No. 064009.
(40) Emtsev, K. V.; Bostwick, A.; Horn, K.; Jobst, J.; Kellogg, G. L.; Ley, L.; McChesney, J. L.; Ohta, T.; Reshanov, S. A.; Röhrl, J.; et al. Towards Wafer-Size Graphene Layers by Atmospheric Pressure Graphitization of Silicon Carbide. *Nat. Mater.* **2009**, *8*, 203−207.
(41) Badami, D. V. X-Ray Studies of Graphite Formed by Decomposing Silicon Carbide. *Carbon* **1965**, *3*, 53−57.
(42) Dresselhaus, G. Spin-Orbit Coupling Effects in Zinc Blende Structures. *Phys. Rev.* **1955**, *100*, 580−586.
(43) Ganichev, S. D.; Golub, L. E. Interplay of Rashba/Dresselhaus Spin Splittings Probed by Photogalvanic Spectroscopy-A Review. *Phys. Status Solidi B* **2014**, *251*, 1801−1823.
(44) Di Sante, D.; Barone, P.; Bertacco, R.; Picozzi, S. Electric Control of the Giant Rashba Effect in Bulk Gete. *Adv. Mater.* **2013**, *25*, 509−513.
(45) Kamata, Y.; Kurimura, S.; Uesu, Y.; Strukov, B. A. Method for Separating Linear and Circular Photogalvanic Effects and Its Application to Ferroelectric Lead Germanate. *Jpn. J. Appl. Phys.* **1994**, *33*, 5453.
(46) Autieri, C.; Barone, P.; Sławińska, J.; Picozzi, S. Persistent Spin Helix in Rashba-Dresselhaus FerroelectricCsBiNb2O7. *Phys. Rev. Mater.* **2019**, *3*, No. 084416.
(47) Ai, H.; Ma, X.; Shao, X.; Li, W.; Zhao, M. Reversible Out-of-Plane Spin Texture in a Two-Dimensional Ferroelectric Material for Persistent Spin Helix. *Phys. Rev. Mater.* **2019**, *3*, 054407−054414.
(48) Cho, K. S.; Liang, C. T.; Chen, Y. F.; Tang, Y. Q.; Shen, B. Spin-Dependent Photocurrent Induced by Rashba-Type Spin Splitting in Al0.25Ga0.75N/GaN Heterostructures. *Phys. Rev. B* **2007**, *75*, No. 085327.

https://dx.doi.org/10.1021/acs.jpcc.0c00578
J. Phys. Chem. C XXXX, XXX, XXX−XXX